Full-scale observation of the flow downstream of a suspension bridge deck

CrossMark

Etienne Cheynet [a],[*], Jasna Bogunović Jakobsen [a], Jónas Snæbjörnsson [a],[b], Nikolas Angelou [c], Torben Mikkelsen [c], Mikael Sjöholm [c], Benny Svardal [d]

[a] Department of Mechanical and Structural Engineering and Materials Science, University of Stavanger, N-4036 Stavanger, Norway
[b] School of Science and Engineering, Reykjavík University, Menntavegur 1, 101 Reykjavík, Iceland
[c] Department of Wind Energy, Technical University of Denmark, Risø Campus, Frederiksborgvej 399, DK-4000 Roskilde, Denmark
[d] Christian Michelsen Research AS, Fantoftveien 38, Bergen, Norway

ABSTRACT

The paper presents a full-scale observation of the flow conditions downstream of a suspension bridge by a system of synchronized short-range dual-Doppler wind lidars. The lidar units were deployed directly on the bridge walkway during a four-day pilot experiment. The wind velocity was monitored at every meter along a 111 m long vertical line segment 40 m downstream of the deck, with a sampling period of one second. The lidar wind data are studied in terms of the mean wind velocity deficit and turbulence intensity downstream of the bridge deck. They provided a full-scale characterization of the wake of a bridge box girder not previously seen in the literature. This includes an observation of the vortex shedding process, consistent with a Strouhal number of 0.11. The drag coefficient, deduced from the mean velocity deficit, is found to be comparable to the value available from the wind tunnel tests. Challenges in the estimation of the wind velocity data related to the variable measurement noise of the individual lidars, as a function of the wind direction, are highlighted. Suggestions for future applications of a similar measurement set-up, based on this unique study performed during a single day only, are also provided.

1. Introduction

Investigations of wake flow characteristics of a streamlined closed-box bridge girder have been mostly limited to scaled model (Fransos and Bruno, 2010; Chen et al., 2014; Yang et al., 2015) or numerical analysis (Fujiwara et al., 1993; Kuroda, 1997). In full-scale, the flow around a bridge girder can be studied using the pressure distribution around the deck (Frandsen, 2001; Li et al., 2014), but the analysis of the downstream flow may not be possible without the use of remote sensing technology.

The measurement of the turbulent wake behind structures in full-scale using optical remote sensing technology, and in particular scanning Doppler Wind lidars, has become increasingly popular during the last 10 years. Until now, wind turbines are the most commonly studied structures (Table 1). Both pulsed lidars and continuous-wave (CW) lidars have been used for this purpose. Pulsed lidars offer the possibility to study simultaneously the near and far wake, but with a relatively low temporal resolution. In the studies of Käsler et al. (2010), Iungo et al. (2013) or Aitken et al. (2014) for example, the sampling period from which the wind statistics are derived using a single lidar is at least 20s,

which mainly limits their analysis to the mean wind velocity.

The use of a CW lidar allows to scan the flow at a much larger sampling frequency and a higher spatial resolution than a pulsed lidar, although the maximal scanning distance is lower, i.e. about 200 m. One of the first successful applications of CW lidar to monitor the turbulent wake comes also from the field of wind energy with the nacelle-mounted lidar (Bingöl et al., 2010). In such a configuration, a CW lidar is located on the back of the nacelle of a wind turbine and measures the flow downstream to the turbine. Bingöl et al. (2010) used for example a Line Scan Mode (LSM) for that purpose, where the flow is measured with a constant focus distance along a single arc, whereas Trujillo et al. (2011) investigated the two-dimensional wake using a Sphere Scan mode (SSM). More generally, an increasing complex scanning pattern is associated with a decreasing temporal resolution, which is one of the reasons why Table 1 shows that CW lidars have been used with a large variety of sampling periods.

Only the along-beam wind component, also called line-of-sight (LOS) component, can be retrieved using a single wind lidar. This limits a more in depth study of the wake behind a large structure. At small elevation angles, two lidars can be used simultaneously to retrieve the two

---

Table 1
Previous full-scale measurements of the wake behind a single structure using scanning Doppler wind lidar technology. The sampling period is defined here as two times the duration required to complete one scanning pattern.

Reference	Structure	sampling period (s)	Lidar type	Number of lidars
Käsler et al. (2010)	Wind turbine	28–44	Pulsed	1
Iungo et al. (2013)	Wind turbine	82	Pulsed	1
Aitken et al. (2014)	Wind turbine	20–40	Pulsed	1
van Dooren et al. (2016b)	Wind turbine	48	Pulsed	2
Bingöl et al. (2010)	Wind turbine	3.2	CW lidar	1
Trujillo et al. (2011)	Wind turbine	2.2	CW lidar	1
Peña et al. (2016)	Fence	42	CW lidar	3
Present study	Bridge deck	1.0	CW lidar	2

horizontal wind components (Newsom et al., 2008; van Dooren et al., 2016b, a). In some cases, a scan can be conducted in a vertical plane aligned with the wind direction, as done by Iungo et al. (2013), who briefly explored the possibility of using a dual-lidar system to measure the vertical and along-wind component in the wake of a wind turbine. The three wind velocity components can be directly retrieved using three synchronized Doppler wind lidar units (Mann et al., 2009; Fuertes et al., 2014), provided that the different scanning beams cross with angles large enough, i.e. as close as possible to 90°. Scanning strategies involving multiple CW lidar are less common than those involving pulsed lidars. To the authors' knowledge, the short-range WindScanner system (Mikkelsen, 2014), developed at the Department of Wind Energy at the Technical University of Denmark (DTU) Risø campus, is currently the only system using two or three synchronized CW lidar units.

The possibility to explore the interactions between the natural wind and wind-exposed structures using Doppler lidar technology is not limited to wind turbines. A pilot study on the applicability of lidars for assessment of wind conditions on a bridge site was performed at the Lysefjord Bridge in Norway, in 2014 (Cheynet et al., 2016, 2017). The present paper explores the flow disturbed by the bridge girder, through wind velocity data recorded 40 m downstream of the bridge. To the authors' knowledge, no comparable full-scale measurement has been performed before, making the data set in question unique.

Measurement of the flow downstream of a bridge deck using Doppler wind lidars is challenging because of the presence of a non-uniform vertical mean wind velocity profile and an upstream flow with a varying velocity and direction, which the researcher cannot control. These challenges are addressed in the present study, which has the primary goal of demonstrating how the short-range WindScanner system can be used to achieve a better understanding of the flow around full-scale large civil engineering structures.

In the following, the monitoring system and the scanning modes used are described first. The data analysis is presented in terms of a flow "visualization" and in terms of the wind velocity statistics. Finally, the current challenges and future configurations facilitating an improved description of the turbulent wake of a bridge deck are discussed.

2. Monitoring system and methods

The Lysefjord suspension bridge was built in 1997 on the south-west of the Norwegian coast between high cliffs at the inlet of a deep and narrow fjord (Fig. 1). The bridge has a main-span of 446 m and a hexagonal closed box girder, with height H of 2.76 m and width B equal to 12.3 m. The girder is asymmetric with respect to the x-axis (Fig. 2). The bridge is oriented from north-west to south-east and is mainly subjected
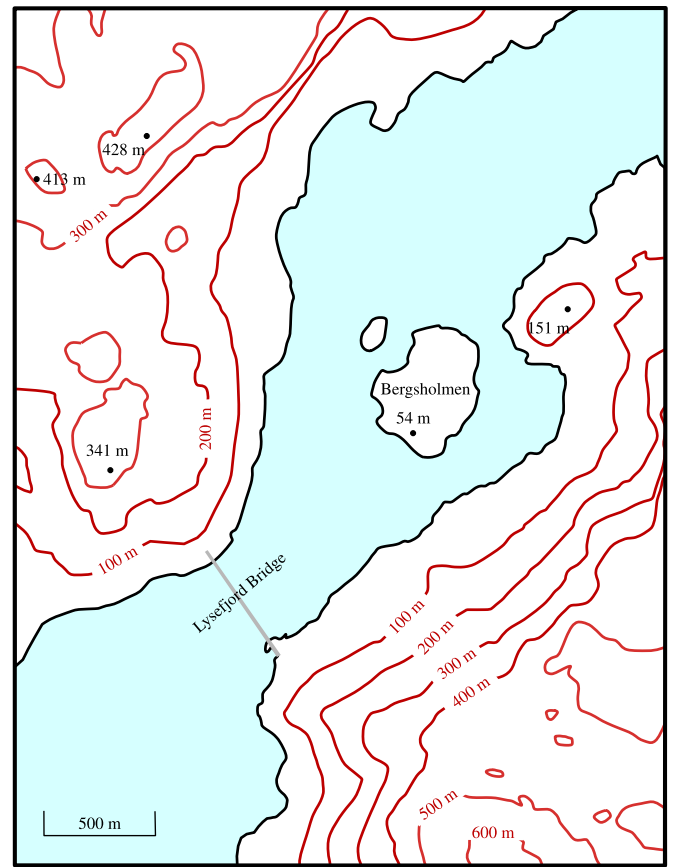

Fig. 1. Simplified topographic map of the inlet of the Lysefjord reproduced from www. norgeskart.no.

to two wind directions, north-northeast (N-NE) and south-southwest (S-SW), where the N-NE direction represents the flow from the inside of the fjord.

The three wind velocity components are here denoted u, v and w, where u is the along-wind component, v is the crosswind component and w is the vertical component. The so-called along-beam wind component v_r results from the projection of the three-dimensional wind velocity vector onto the scanning beam of the lidar. Each velocity component can be decomposed into a mean component, denoted by an overline and a fluctuating component with zero mean denoted by a prime:

$$u = \overline{u} + u' \tag{1}$$

$$v = \overline{v} + v' \tag{2}$$

$$w = \overline{w} + w' \tag{3}$$

$$v_r = \overline{v_r} + v_r' \tag{4}$$

where $\overline{v} = \overline{w} = 0 \text{ m s}^{-1}$ (Teunissen, 1980). Unless the scanning beam is perpendicular to the mean flow, the mean velocity of the along-beam component verifies $\overline{v_r} \neq 0 \text{ m s}^{-1}$. In the present study, wind statistics are estimated using the standard averaging time of 10 min.

2.1. Long-term instrumentation

In May 2014, five sonic anemometers and three pairs of accelerometers were operating on the Lysefjord bridge. The anemometers are deployed along the west side of the bridge girder, 6 m above the deck,
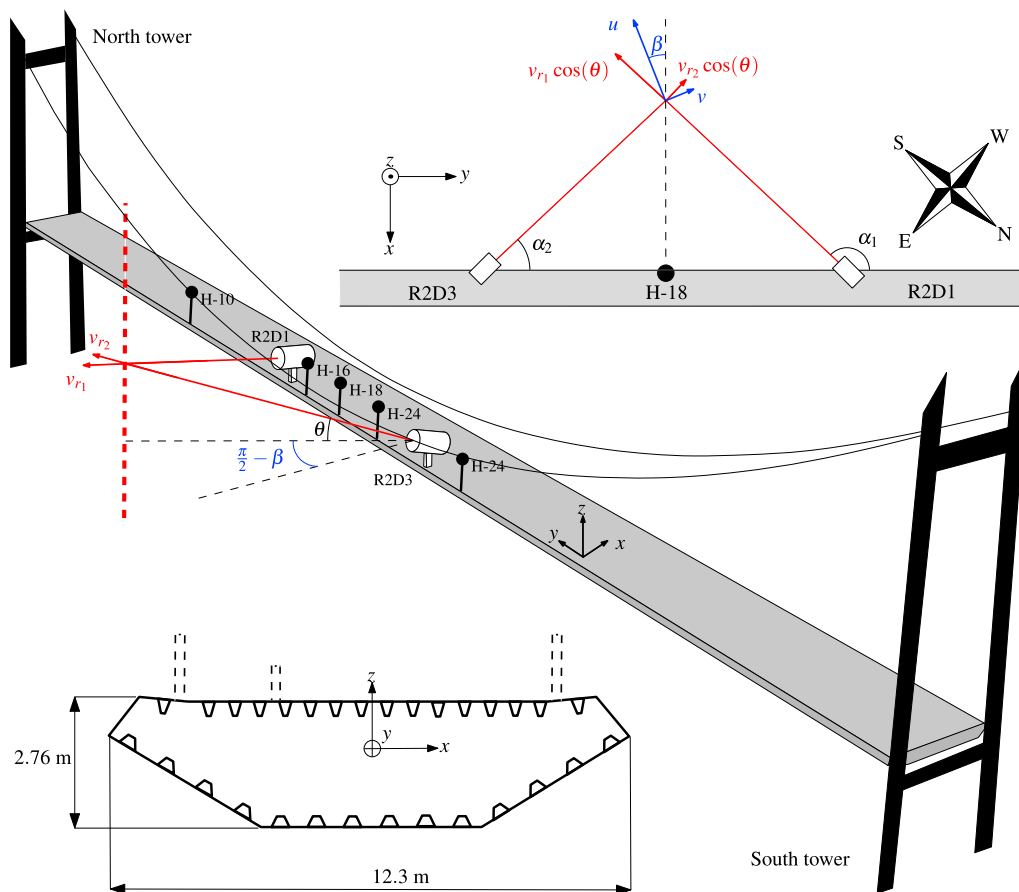
Fig. 2. Schematic of the dual-lidar scanning system (R2D1 and R2D3) monitoring the flow near H-18. Hangers are not drawn and the scales are not respected for the sake of clarity.

near hangers 10, 16, 18, 20 and 24, denoted H-10, H-16, H-18, H-20 and H-24, respectively. The hanger 18 is located at midspan and the distance between two adjacent hangers is 12 m (Fig. 2). The bridge response data were recorded simultaneously with triaxial accelerometers located near H-16, H-18, and H-20. The wind velocity and bridge acceleration data are synchronized using 3 data logging units located inside the bridge deck and sampled at 20 Hz. A router provides wireless data access and their transfer via a mobile network. A more detailed description of sensors installed on the Lysefjord Bridge is provided in Table 2.

2.2. Short-term instrumentation

The short-range WindScanner system was deployed on the Lysefjord Bridge during four days in May 2014. The WindScanner system used here consists of two synchronized CW coherent wind lidar instruments. The lidar units are modified ZephIR 150 (Natural Power), which are designed upon the principles of the CW coherent laser radar described by Karlsson et al. (2000). Each modified lidar unit is equipped with a 3 inches (7.62 cm) optical lens and a fast-scanning rotating head, allowing a scan

within a cone with a half opening angle of 60°. A more detailed description of the modified lidar units can be found in Sjöholm et al. (2014). Table 3 summarizes the technical specifications of the Wind-Scanner system used here, following the information provided in Sjöholm et al. (2014), Lange et al. (2015) and Cheynet et al. (2016).

The first lidar, named R2D1, was located on the north side of the bridge, 45 m from H-18, whereas the second lidar, named R2D3, was on the south side, 45 m from H-18. The lidar units were deployed on the walkway on the west side of the deck. The first part of the measurement campaign allowed the study of the horizontal flow upstream of the deck (Cheynet et al., 2016) since the wind direction was S-SW. The data provided validation of the lidar wind velocity records, including the wind coherence for the separations along a line parallel to the bridge axis. During the last 8 h of the campaign, the wind direction switched to N-NE and the lidar measured, therefore, the flow disturbed by the deck. The scanning configuration was modified in such a way that the flow was monitored along a 111 m vertical line segment, instead of along a horizontal line parallel to the deck. This vertical line segment was located 40 m downstream of the girder, at mid-distance between the two lidars

Table 2
Long-term instrumentation of the Lysefjord Bridge in May 2014.

Location	Sensor	Brand	Model	Number	Maximum Sampling frequency (Hz)
H-10	Weather Transmitter	Vaisala	WXT520	1	4
H-16	3-D sonic anemometer	Gill instruments	WindMaster Pro	1	32
H-18	3-D sonic anemometer	Gill instruments	WindMaster Pro	1	32
H-20	3-D sonic anemometer	Gill instruments	WindMaster Pro	1	32
H-24	3-D sonic anemometer	Gill instruments	WindMaster Pro	1	32
H-16	3-D accelerometer	Canterbury Seismic Instruments	CUSP-3D	2	200
H-18	3-D accelerometer	Canterbury Seismic Instruments	CUSP-3D	2	200
H-24	3-D accelerometer	Canterbury Seismic Instruments	CUSP-3D	2	200

Table 3
Configuration of the lidar instruments used in the present study.

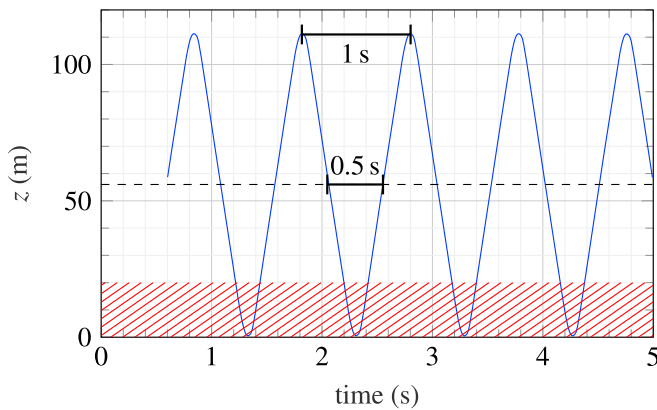| Properties	Short-range WindScanner
Wavelength	1.565 μm
Beam-width (at 40 m range)	<1 mm
Probe length (at 40 m range)	2.0 m
Pointing accuracy	0.1°
Synchronization uncertainty	1.7 m s
Shortest range	8 m–10 m
Longest range	150 m–200 m
LOS sampling frequency	390 Hz
Lidars LOS detection range	-21 m s^{-1} to $+18$ m s^{-1}

Fig. 3. First five seconds of the trajectory (solid line) of the scanning volume. The dashed line corresponds to the height at which the lidars are located: The hatched area denotes the domain that is not reached by the beams, due to their intersection with the deck.

(Fig. 2), and the elevation angles ranged, therefore, from $-43°$ to $+43°$.

Fig. 3 shows that the trajectory of the volume corresponding to the intersection of the two scanning beams is almost a triangular waveform when displayed as a function of the time. In Fig. 3, the altitude corresponding to a zero elevation angle is shown as a dashed line, whereas the hatched area corresponds to the first 20 m above the mean sea level where the wind velocity is not measured due to the intersection of the laser beams with the deck. The scanning beams need 0.5s to travel along the 111 m line segment. In the central part of the line segment, i.e. at a zero elevation angle, wind velocity data are retrieved with a uniform sampling frequency of 2 Hz. At the uppermost and lowermost boundary of the line segment, i.e. at $z = 0.5$ m and $z = 111$ m (see Fig. 3), the sampling frequency drops down to 1 Hz. To simplify the data processing, the wind velocity records are, therefore, re-sampled using linear interpolation with a uniform sampling frequency of 1 Hz.

2.3. Retrieval of the horizontal wind components

At the bridge site, the wind direction is often observed to be skewed with respect to the deck. The yaw angle, defined as the angle between the wind direction and the normal to the deck is denoted β. In Fig. 2, the WindScanners R2D1 and R2D3 target their focus on the same point in space, but actually, the two lidars measure the line-of-sight wind component of the 3D wind velocity vector weighted in a volume stretched along the light-beam. For CW lidars, the volume size increases proportionally with the distance squared from the instrument (Sjöholm et al., 2009). Consequently, the volumes in which the lidars measure the flow do not necessarily have the same dimensions or perfectly overlap one another. Measurements are averaged in each volume, which implies a spatial low-pass filtering of the higher frequency components. This was previously studied for the WindScanner by e.g. Angelou et al. (2012b), and is referred to herein as the "spatial averaging effect".

The lowest range resolution of the short-range WindScanner system used here corresponds to the longest sampling volume equal to ca.

8.6 m at the longest scanning distance of 82 m. Although the Full Width at Half Maximum (FWHM) of each lidar unit fluctuates between 4.6 m and 8.6 m during the particular set-up, the volumes are partially overlapping, which allows in the present case the selection of the velocity data with a vertical spatial resolution of ca. 1 m.

The two line-of-sight wind records obtained from R2D1 and R2D3 are denoted v_{r_1} and v_{r_2}, respectively. The relation between the line-of-sight wind velocity components and the horizontal and vertical ones is given here as a system of two equations with three unknowns:

$$\begin{bmatrix} v_{r_1} \\ v_{r_2} \end{bmatrix} = \mathbf{R} \times \begin{bmatrix} u \\ v \\ w \end{bmatrix} \tag{5}$$

where the matrix $\mathbf{R}$ is:

$$\mathbf{R} = \begin{bmatrix} \sin(\beta + \alpha_1)\cos(\theta) & \cos(\alpha_1 + \beta)\cos(\theta) & \sin(\theta) \\ \sin(\beta + \alpha_2)\cos(\theta) & \cos(\alpha_2 + \beta)\cos(\theta) & \sin(\theta) \end{bmatrix} \tag{6}$$

where α_1 and α_2 are the angles between the projection of the laser beam onto the horizontal plane and the deck orientation. In the present case, α_1 and α_2 are fixed and equal to 38° and 42°, respectively. R2D3 points, therefore, toward west, and R2D1 points toward south. The elevation angle θ is defined as the angle between the laser beam and its projection onto the horizontal plane (Fig. 2).

Methods to retrieve the three wind components from dual scan data have recently been developed. Newsom et al. (2015) used intersecting scanning planes from a system of dual pulsed lidars combined with the continuity equation for incompressible flow to retrieve the three wind components. For elevation angles up to 30°, they observed that the vertical component retrieved this way had only a small impact on the horizontal components. Here, such a method cannot be applied because the flow is scanned along a single vertical line segment only. Moreover, we focus on the bridge wake, where the elevation angle is relatively small, which allows additional assumptions. The wind components u and v can be retrieved if θ is small enough to be neglected, so that the number of unknowns in Eq. (5) reduces to two. If the wind direction measured by the sonic anemometer on H-18 is more or less the same 40 m downstream of the deck, the mean wind velocity $\bar{u}$ can be directly retrieved from a single lidar using Eq. (5). The relative error due to the assumption of negligible influence of the vertical wind component on the horizontal flow has to be investigated if the root mean square (RMS) of the wind fluctuations is to be studied. The error done using the approximation

$$\sigma_{v_r}^{\text{approx}} \approx \sigma_u \sin(\alpha + \beta)\cos(\theta) + \sigma_v \cos(\alpha + \beta)\cos(\theta) \tag{7}$$

is investigated assuming that $\sigma_v = 0.8\sigma_u$ and $\sigma_w = 0.6\sigma_u$. The coefficients 0.8 and 0.6 are here arbitrarily chosen, so that the relative error on σ_{v_r} can be considered as conservative, while being in the range of expected values for undisturbed flow conditions (Solari and Piccardo, 2001). In the turbulent wake of a bridge, the ratios σ_v/σ_u and σ_w/σ_u are unknown and the values adopted here are used in a first approximation only. The resulting relative error is:

$$\varepsilon_i = \frac{0.6\sin(\theta)}{\sin(\alpha_i + \beta)\cos(\theta) + 0.8\cos(\alpha_i + \beta)\cos(\theta) + 0.6\sin(\theta)} \tag{8}$$

where ε_1 and ε_2 are the relative errors obtained for the R2D1 and R2D3 velocities, respectively. In Fig. 4, ε_1 and ε_2 are expressed as a function of the altitude and the yaw angle. The yaw angles are bounded between 20° and 40° to include the majority of values measured during the period of study. Fig. 4 shows that a larger error is obtained for negative elevations angles and for the lidar R2D1. For the lidar R2D1, the vertical component leads to an error varying between 11% and 15% at $z \approx 45$ m. At $z \approx 65$ m, the relative error is lower, with values ranging from 7% to 10%.
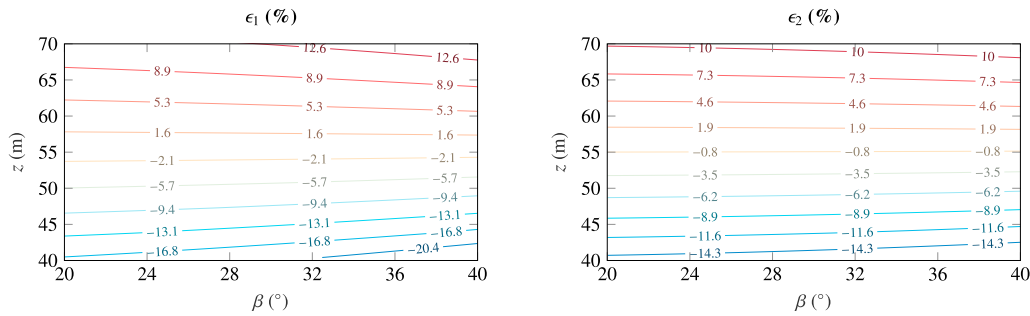
Fig. 4. Error induced on the RMS of the along-beam wind velocity at each lidar by disregarding the vertical wind component.

2.4. Atmospheric stability

The atmospheric stability is estimated using the Obukhov length (Obukhov, 1946), defined as:

$$L = -\frac{\overline{\theta_v} u_{*_0}^3}{g\kappa \left(\overline{w\prime\theta_v\prime}\right)_0} \tag{9}$$

where $\left(\overline{w\prime\theta_v\prime}\right)_0$ is the surface flux of virtual potential temperature; $\overline{\theta_v}$ is the mean virtual potential temperature; g is the gravitational acceleration; $\kappa \approx 0.40$ is the von Kármán constant and u_{*_0} is the surface friction velocity. According to the Monin-Obukhov similarity theory, u_* and $\overline{w\prime\theta_v\prime}$ are invariant with height in the surface layer. Although the sonic anemometers are located ca. 62 m above the sea level, they are surrounded by mountains. The measurements were, therefore, assumed to be conducted in the surface layer, and the vertical fluxes of heat and momentum were estimated locally, using the sonic temperature recorded on H-18 and an averaging period of 10 min:

$$u_{*_0} \approx u_* \tag{10}$$

$$\left(\overline{w\prime\theta_v\prime}\right)_0 \approx \overline{w\prime\theta_v\prime} \tag{11}$$

where u_* is calculated as:

$$u_* = \left(\overline{u\prime w\prime}^2 + \overline{u\prime v\prime}^2\right)^{1/4}. \tag{12}$$

The sonic temperature is here assumed to be equal to the virtual temperature. The virtual potential temperature was estimated by combining the sonic temperature and the atmospheric pressure data recorded by the Vaisala weather station on H-10. It should, however, be noted that during the measurement period, the atmospheric pressure was about the same as the standard pressure.

2.5. Drag coefficient

By using the conservation of momentum and the measure of the velocity deficit downstream of the bridge, the drag coefficient of the deck can be estimated:

$$Cd = \frac{2}{H\overline{u}_0^2} \cdot \int_{z_1}^{z_2} \overline{u}(z) \cdot [\overline{u}_0 - \overline{u}(z)] \, dz \tag{13}$$

where H is the deck height and $\overline{u}_0$ is the undisturbed mean wind velocity. The assumption of uniform vertical upstream flow is usually a prerequisite for Eq. (13), but is not valid in the atmospheric boundary layer. To limit the divergence from this assumption, the integration domain is limited between two reference altitudes z_1 and z_2, that "define" the boundaries of the wake. The value $z_2 - z_1$ must be large enough to encompass the full width of the wake but also small enough to satisfy the requirement of small elevation angles so that the horizontal wind

components can be properly retrieved (cf. subsection 2.3). In the present calculation of Eq. (13), the integration domain is smoothed by using a piecewise cubic spline with eight knots to reduce the error due to the relatively coarse spatial resolution $\Delta_z = 1$ m between z_1 and z_2. The use of a relatively high number of knots allows here a more accurate capture of the vertical velocity profile in a sheared flow. The value of $\overline{u}_0$ is approximated as the average between the mean wind velocity recorded by the WindScanners at the two reference altitudes z_1 and z_2.

2.6. Data processing

The algorithm proposed by Wilczak et al. (2001) is applied to correct any possible error in the estimation of u_* and $\overline{w\prime\theta_v\prime}$ due to the tilt angles of the anemometers. This algorithm is based on a planar fit that is applied using all the samples recorded by the sonic anemometer on H-18 between 01:00 and 10:00 on 23/05/2014 (41 samples). Finally, outliers in the time series recorded by the sonic anemometer on H-18 are removed using a Hampel filter (Pearson, 2005), with a window length of 240s and 5 standard deviations away from the local median. Because the wind velocity data recorded by the lidars contains more outliers than those recorded by the anemometer on H-18, a Hampel filter with a window length of 40s and 3 standard deviations away from the local median is applied to the lidar measurements.

3. Results

3.1. Normalized Doppler spectrum maxima

To assess the signal quality, the Normalized Doppler Spectrum Maximum (NDSM), which is provided along with the corresponding velocity estimation is used. The NDSM is defined as the maximum of the Doppler spectrum normalized with the mean background noise spectrum (Angelou et al., 2012a). The NDSM depicts the intensity of the backscattered signal in the dominant Doppler frequency. Moving hard targets will result in a high maximum value, while non-moving hard targets will not be detected. The NDSM is denoted S_{R2D1} and S_{R2D3}, for each lidar unit, respectively.

To facilitate the comparison between S_{R2D1} and S_{R2D3} and improve their visualization, the NDSM of each lidar is divided by $\overline{S_0}$, where $\overline{S_0}$ is the NSDM of the lidar R2D1 averaged over the measurement height and the time. In the present case, $\overline{S_0}$ is equal to 1.39. The lidar R2D1 is chosen here as the reference lidar because it provides in the present case larger NDSM than the lidar R2D3. To improve the visualization of the normalized spectral maxima, the pseudocolor plot displayed in Fig. 5 uses a diverging delta color map (Thyng et al., 2016). Finally, S_{R2D1} and S_{R2D3} have been smoothed using a moving average filter in the horizontal direction with a hamming window of width 60 s. In the present study, data with a NDSM lower than a threshold value $S_{thres} = 1.17$ were disregarded. This threshold value is arbitrarily defined and corresponds to the ratio $S_{thres}/\overline{S_0} = 0.84$.

Fig. 5 shows that for the measurement period considered, the data

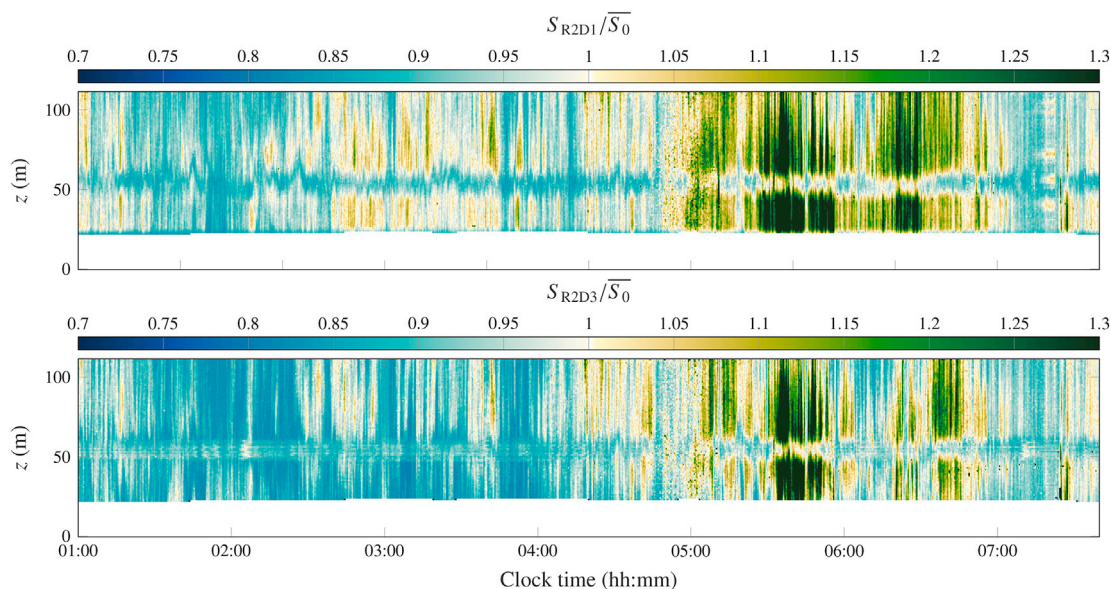**Fig. 5.** Evolution of the ratios $S_{R2D3}/\overline{S_0}$ and $S_{R2D1}/\overline{S_0}$ with the measurement height and the time for the lidar R2D1 (top) and R2D3 (bottom) on 23/05/2014, where S_{R2D1} and S_{R2D3} are the NDSM of the lidar R2D1 and R2D3, respectively; $\overline{S_0}$ is the NDSM of the lidar R2D1 averaged over the measurement period and the measurement height.

recorded by the lidar R2D1 are in general of better quality than those recorded by the lidar R2D3. The lower-than-average data quality of both lidar units is clearly visible before 04:00. In the case of the lidar R2D3, the ratio $S_{R2D3}/\overline{S_0}$ is often below 0.84, indicating a reduced data availability. For both lidar units, the NDSM is lower within the bridge wake. Consequently, the ratio $S_{R2D3}/\overline{S_0}$ and $S_{R2D1}/\overline{S_0}$ are most of the time below 1 at heights between 50 m and 60 m. This is explained by the fact that a more turbulent flow or a flow with a gradient within the measurement volume broadens the Doppler spectra and spreads out the power over a wider frequency range, thus reducing the peak signal power. Nonetheless, the ratio $S_{R2D1}/\overline{S_0}$ is in general good enough so that the low-frequency fluctuations of the wake are clearly visible at heights ranging from 50 m to 60 m. The ratio $S_{R2D3}/\overline{S_0}$ shows, however, a noisy pattern in the wake area from 01:00 to 04:20, which suggests that the NDSM is too low to allow a proper retrieval of the wind data. From 05:00 to 07:00, the NDSM is significantly larger than during the rest of the measurement period. Furthermore, subsection 3.3 shows that during this period, the best agreement is obtained between the sonic anemometer data at mid span and the lidar data. More generally, Fig. 5 presents how the NDSM may be used to study the flow around structures.

The fluctuating pattern observed near $z = 55$ m in Fig. 5 is unlikely to be solely due to the presence of the bridge deck. Firstly, because some fluctuations show a temporal scale of several minutes, i.e. much larger than those that may be induced by the motion of the bridge deck.

Secondly, because the wake can be detected up to 20 m above the girder location, which is unusually large compared to the deck height, which is only 2.76 m. A more detailed discussion of the possible origin of this phenomenon is provided in subsection 3.5.

3.2. Flow visualization

The Obukhov length L is calculated using Eq. (9) and the data recorded by the sonic anemometer on H-18. On 23/05/2014, between 01:00 and 07:50, the median value of the Obukhov length was 56 m, with on average $u_* = 0.24$ m s^{-1} and $\overline{w'\theta_v'} = -0.019$ K m s^{-1}. From 05:30 to 05:40, which is the period during which the data displayed in Figs. 6–7 are recorded, the Obukhov length is equal to 103 m. The flow studied here corresponds, therefore, to a stable atmospheric stratification. The predominance of such a stratification was already suggested by the low turbulence intensity for the low wind velocity recorded. The average turbulence intensity of the along-wind component measured during the present study was equal to 10.4% for $\overline{u} \geq 5$ m s^{-1}. This situation is exceptional in Lysefjord, where a turbulence intensity above 20% is recorded most of the time for the wind from N-NE (Cheynet, 2016; Chap. 4.2). A stable stratification facilitates the study of the flow around structures as it limits turbulent mixing. The occurrence of these wind conditions at the time of deployment of the WindScanner system was fortunate, as it simplified the study of the wake of the bridge.
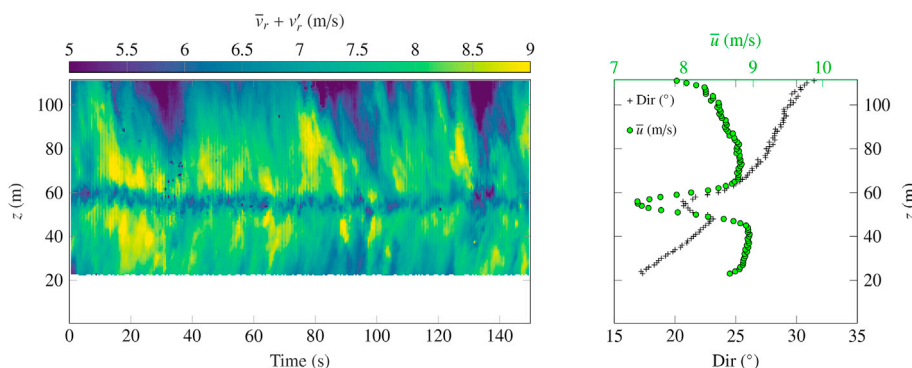

Fig. 6. Left: Radial wind velocity recorded by R2D1 during the vertical scan on 23/05/2014 from 05:30. Right: Vertical profiles of the mean wind velocity and the mean wind direction evaluated using the lidars measurements between 05:30 and 05:40.
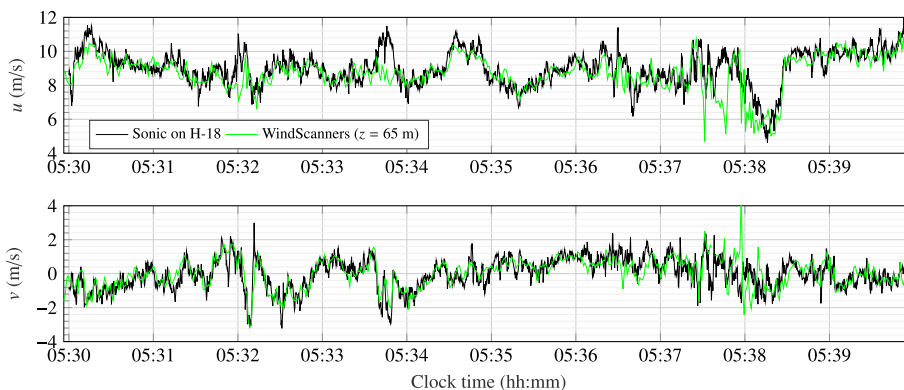
Fig. 7. Along-wind and crosswind components recorded by the anemometer on H-18 and the WindScanners slightly above the bridge wake.

To illustrate the ability of a short-range scanning lidar to capture turbulent flow with a high temporal and spatial resolution, the along-beam wind velocity recorded from 05:30 by the WindScanner R2D1 along a vertical line segment is shown on the left panel of Fig. 6. The darker area centered around $z \approx 56$ m corresponds to the recorded turbulent wake, associated with a clear velocity deficit in the wake area (right panel of Fig. 6). The unusual vertical profile observed may be due to topographic effects, such as the narrowing of the fjord at the lower elevations, as the flow approaches the bridge. A 54 m high island, called Bergsholmen, located 1 km to the north-east of the bridge, also contributes to the rather complex flow conditions at the bridge site. The wake of the bridge may, therefore, be influenced by the vertical profile of the wind velocity, including the wake of the island. On Fig. 6, the wind direction increases from 18° at 24 m to 32° at 110 m, which also suggests a dependency of the velocity profile on the yaw angle β.

A closer look at Fig. 6 (left panel), shows a clear oscillating pattern of the along-beam wind velocity with a period of about 3s, especially during the first 30s. The velocity data indicates an intermittent, broad-banded vortex shedding process. The oscillatory character of the vortex shedding process is visualized by the cross-flow fluctuations of the wake "centre", i.e. the area associated with the largest velocity deficit. The geometry and aspect ratio ($B/H \approx 4.5$) of the Lysefjord Bridge deck cross section is similar to the one studied in a wind tunnel by Hjorth-Hansen (1987), of which the vortex shedding associated with the Strouhal number of $S_t = 0.11$ was observed. The Strouhal number S_t is defined as:

$$S_t = \frac{fD}{\bar{u}}. \tag{14}$$

In Eq. (14), D is a typical dimension of the structure considered, e.g. the height of the deck in the present case. The Strouhal number of 0.11 applied to the incoming velocity of 9 m s^{-1} and the deck height $H = 2.76$ m indicates a vortex shedding frequency of 0.36 Hz, which is in agreement with the observed wake oscillation period of ca. 3s.

Fig. 7 displays 10 min of wind velocity data recorded from 05:30 to 05:39 by the WindScanner system and the sonic anemometer on H-18. The wind components u and v recorded by the WindScanners agree well with those obtained with the anemometer. The altitude of the lidar's record is taken as 65 m, which is about 3 m above the sonic anemometers position. For the selected sample, the mean yaw angle is $\beta = 25°$ and its standard deviation is 5.7°. At this altitude, the flow seems to be relatively unaffected by the wake of the bridge. The WindScanner R2D3 was measuring in a direction almost perpendicular to the flow during this period, and since the estimation of the line-of-sight velocity from the Doppler spectra has a higher uncertainty in the vicinity of 0 m s^{-1}, some outliers were observed. In addition, the NDSM of the R2D3 WindScanner was generally lower due to lower laser power output, which led to a lower data availability.

Time-histories of the bridge vertical acceleration response

corresponding to flow conditions presented in Fig. 6, i.e. between 05:30 and 05:32, are displayed on the top panel of Fig. 8. The bottom panel shows a time-frequency description of the bridge acceleration response using the Evolutionary Power Spectral Density (Priestley, 1965). During the first 40s, the bridge response is dominated by a single mode of vibration with a frequency around 0.3 Hz, which corresponds to the first vertical symmetric eigenmode VS1 ($f_{VS1} = 0.298$ Hz). This frequency compares reasonably well with the 3s period seen in the flow. After 30s, the second vertical symmetric eigenmode, denoted VS2 ($f_{VS2} = 0.405$ Hz) becomes noticeable, and both VS1 and VS2 remain visible during the rest of the record. A more "noisy" response recorded from 60s to about 90s is due to the contribution of higher modes at 2.4 Hz, 3.3 Hz and 4.3 Hz, and indicates the traffic-induced vibrations. The interval is consistent with the time it takes for a vehicle to cross the 446 m long bridge span at the speed of 50 km h^{-1}. The fact that the vertical motion of the bridge deck is affected by higher modes of vibration after 05:30:20, slightly diffuses the otherwise clear oscillating pattern in the left panel of Fig. 6.

3.3. Statistical moments

The comparison presented in Fig. 7 is extended by Fig. 9, which displays the 10-min mean wind velocity and the turbulence intensity of the along-wind and crosswind components, recorded on 23/05/2014 from 01:00 to 07:50 by the WindScanner system at $z = 65$ m and the sonic anemometer on H-18.
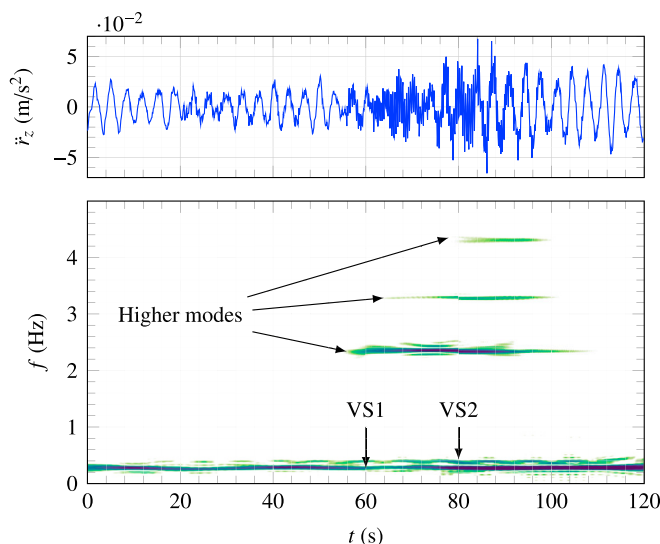

Fig. 8. Vertical bridge acceleration at midspan (top) and corresponding normalized EPSD (bottom) from 05:30:00 on 23/05/2014.
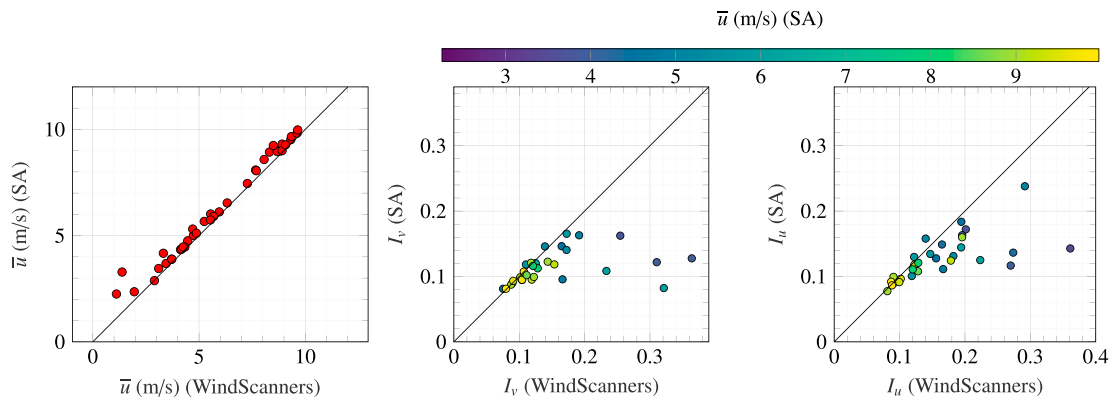
Fig. 9. Mean wind velocity (left panel), crosswind turbulence intensity (middle panel) and along-wind turbulence intensity (right panel) recorded by the WindScanners 65 m above the sea level (horizontal axis), 40 m downstream of the deck, compared to the sonic anemometer (SA) measurements on H-18 (vertical axis). The data used corresponds to the record period spanning from 01:00 to 07:50 on 23/05/2014.

The mean wind velocity recorded by the WindScanner system is on average 7.8% lower than the one recorded by the sonic anemometer on H-18. The turbulence intensity measured by the lidar units is in good agreement with the one measured by the sonic anemometer for $I_u \leq 0.15$ and $I_v \leq 0.15$. The larger discrepancies are due to a low NDSM ratio measured by the lidar R2D3, which propagates into the retrieval of the horizontal wind components. The majority of the large discrepancies observed between the lidar and anemometer measurements are obtained for data recorded before 04:00, i.e. a period during which the mean wind velocity was lower than 5 m s^{-1} on average. For the lidar data recorded after 04:00, the values of $\overline{u}$, σ_u and σ_v estimated at a height of 65 m by the WindScanners differ from the sonic anemometer data by only -4.2%, 2.7% and 2.6%, respectively. An underestimation of I_u and I_v by the lidar instruments is expected, due to the along-beam spatial averaging effect. The existence of a positive relative error in Fig. 4, ranging from 7% to 10% at $z = 65$ m, may cancel out the spatial averaging effect and be responsible for the slight overestimation of I_u and I_v. Another source of discrepancy may also be higher turbulence levels observed by the lidars in the occasionally broader wake and/or the presence of measurement noise from the lidar R2D3 that propagates in the estimation of I_u and I_v, even though the NDSM of the lidar R2D3 is larger after 04:00.

In Fig. 10, the mean velocity $\overline{u}$ and the standard deviations σ_u and σ_v are normalized with the undisturbed mean velocity $\overline{u}_0$ and studied as a function of the measurement height z. The value of $\overline{u}_0$ is estimated as the average between the mean wind velocity in two volumes slightly outside the wake of the deck, i.e. at 43 m and 67 m. The choice of two measurement heights is justified by the need to account for the non-uniformity of the vertical wind profile, which is usually uniform in laboratory experiments, but not in full-scale.

Samples characterized by a high turbulence intensity and/or a lower wind velocity may indicate non-stationary flow conditions, which are partly responsible for a larger scatter of the vertical profiles. In the case of the lidar wind records, samples displaying a high turbulence intensity are also those which disagree the most with the sonic anemometer measurements (Fig. 9). Consequently, samples characterized by $I_u \geq 0.14$ and $\overline{u} \leq 5.0$ m s^{-1} were disregarded in the present case. This results in the selection of 18 samples of 10 min duration, with a turbulence intensity ranging from 0.08 to 0.14 and a wind velocity ranging from 7.7 m s^{-1} to 9.8 m s^{-1}. These samples correspond to a recording period from 04:00 to 07:50 on 23/05/2014.

In Fig. 10, the vertical profiles of $\overline{u}/\overline{u}_0$ and $(\sigma_u/\overline{u}_0)^2$ show strong similarities with those found by e.g. Ong and Wallace (1996) or Narasimhamurthy and Andersson (2009). The averaged profile of $(\sigma_v/\overline{u}_0)^2$ shows, however, an asymmetric feature, possibly due to the absence of the deck symmetry with respect to the x-axis.

The dispersion of the measured velocity profiles increases significantly between $z = 50$ m and $z = 60$ m, i.e. in the wake of the bridge deck. For example, the average value of $\overline{u}/\overline{u}_0$ at $z = 55$ m is around 0.8, whereas the standard deviation is equal to 0.06. A larger dispersion may partly be due to the sensitivity of the velocity deficit profile to the turbulence intensity, the distance at which the wake is recorded, and the low NDSM ratio when the WindScanners are scanning the flow inside the bridge wake. If the turbulence intensity threshold, equal to 0.14 in Fig. 10, is reduced to 0.12, the mean velocity profile $\overline{u}/\overline{u}_0$ is almost unchanged, whereas $(\sigma_u/\overline{u}_0)^2$ clearly moves toward lower values. At $z = 55$ m, $(\sigma_u/\overline{u}_0)^2$ decreases for example from 0.020 to 0.018, which highlights the sensitivity of $(\sigma_u/\overline{u}_0)^2$ to the turbulence intensity threshold.

3.4. Drag coefficient

The drag coefficient is estimated using Eq. (13) and the same data set as in Fig. 10, i.e. 18 samples characterized by $0.08 \leq I_u \leq 0.14$ and 5.2 m s$^{-1} \leq \overline{u} \leq 9.8$ m s^{-1}, where I_u and $\overline{u}$ are the average values
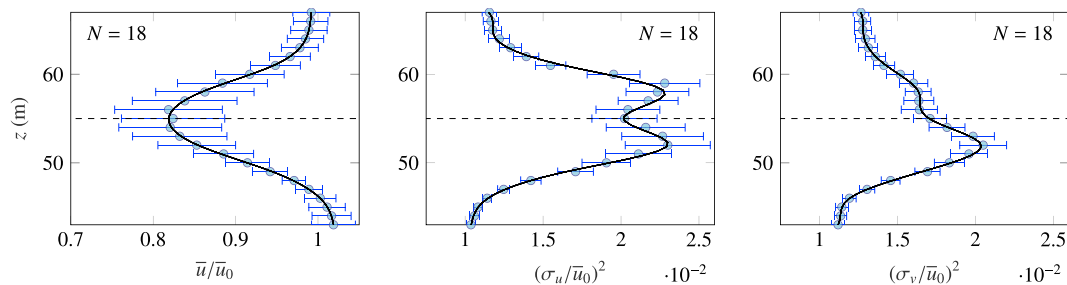

Fig. 10. Vertical profiles of the mean wind velocity and standard deviation of the wind velocity from 43 m to 67 m, corresponding to $0.08 \leq I_u \leq 0.14$ and 5.2 m s$^{-1} \leq \overline{u} \leq 9.8$ m s^{-1} at $z = 67$ m and $z = 43$ m. The averaged data are displayed as a scatter plot with horizontal errorbars representing two standard deviations. The solid black line is a piecewise cubic spline (—) fitted to the averaged data. The position of the deck centre is indicated by a horizontal dashed line (- - -) and the number of samples used is denoted N.

measured at $z = 67$ m and $z = 43$ m by the WindScanners. Eq. (13) is computed using the deck height $H = 2.76$ m as reference dimension; $\overline{u}_0$ is calculated as the average between the mean velocity at $z = 43$ m and $z = 67$ m. The width of the wake $\Delta_z = z_2 - z_1$ is assumed to vary between 10 m and 20 m because it is not precisely known. The average drag coefficient is, therefore, estimated for different values of Δ_z. On Fig. 11, the drag coefficient C_d is displayed as a function of the undisturbed mean wind velocity $\overline{u}_0$ (top panel), the yaw angle β (middle panel) and Δ_z (bottom panel). In the bottom panel, $\overline{C}_d$ denotes the averaged value of C_d, estimated for all wind directions and turbulence intensities, and the associated error bar has a length corresponding to two standard deviations.

As expected for such a sharp edged cross-section, the drag coefficient shows little dependence on $\overline{u}_0$, but decreases for increasing yaw angles, in agreement with the observations of Zhu et al. (2002). The drag coefficient C_d for the Lysefjord bridge deck was for design purposes set equal to 1.0, and its derivative equal to zero. In the present case, the averaged drag coefficient is estimated, with values ranging from 0.88, if the wake width is assumed to be equal to 10 m, to 1.08, if the wake width is 20 m. Although the estimated $\overline{C}_d$ values are in a fairly good agreement with the design value, the latter was adopted for a zero yaw angle, which is not the case in the data set considered. At zero yaw angle, Hjorth-Hansen (1987) estimated a C_d value of about 0.8–0.9, which might be more realistic.

The large variability of the C_d values in Fig. 11 is due to a general variability of the wake width under changing atmospheric conditions, but also to topographic effects on the flow. The middle panel of Fig. 11 shows that yaw angles from $15°$ to more than $40°$ were observed. For $25° \leq \beta < 40°$, the fetch is 2 km and the flow is likely channelled through the fjord when the atmospheric stratification is stable. If $10° \leq \beta < 25°$, the wind field passes over islands, so that the fetch is only 1 km. This results in a complex flow, the turbulent properties of which may change abruptly with relatively small variations in the wind direction. In addition to a challenging application of Eq. (13) in the flow conditions encountered, slightly higher observed C_d values may be due to the contribution of the drag force on the main cables, which approach the deck elevation toward the centre of the bridge span.

3.5. Wind spectra

The one-sided single-point spectra of the along and crosswind components are calculated from 10 min time series using wind velocity data recorded from 01:00 to 07:50 on 23/05/2014 and the periodogram power spectral density (PSD) estimate with a hamming window. This is equivalent to the particular case of Welch's algorithm (Welch, 1967) with a single segment. The choice of using a single segment allows an investigation of the PSD estimate down to a frequency of 0.0017 Hz, but with a relatively large random error. To reduce the random error, the spectra are smoothed in the high-frequency range using block averaging. In addition, the spectra are pre-multiplied with the frequency f, normalized with the variance of the corresponding wind velocity component, and ensemble averaged. This results in a single velocity spectrum estimate, at each height, that is expressed as a function of the reduced frequency:

$$f_r = \frac{fH}{\overline{u}} \tag{15}$$

Data recorded using lidar devices are usually more affected by outliers or missing data points than using sonic anemometers. In the present case, time series with more than 10% of missing data or a standard deviation σ_u measured at $z = 65$ m that differs by more than 10% from the one measured by the sonic anemometer on H-18 are dismissed. This results in 15 available time series at $z = 65$ m and $z = 62$ m, as well as 11 time series at $z = 61$ m. The data availability is, therefore, lower for the computation of the wind spectra S_u and S_v than for the estimation of $\overline{u}$, σ_u and σ_v.

For undisturbed flow conditions, the high-frequency range of the wind velocity spectrum measured by the lidars is expected to be lower than the one estimated from the sonic anemometer data because of the spatial averaging effect (Angelou et al., 2012b). In the present case, Fig. 12 shows that for $f_r \geq 0.03$, the S_u spectrum estimated using the sonic anemometer data on H-18 is only slightly above the one estimated by the lidars at $z = 65$ m. This difference is within measurement uncertainty, as shown by the error bar of the spectrum measured on H-18. This error bar, which has a width of one standard deviation, corresponds to both the random error from block averaging and from ensemble averaging of the different spectra. A more detailed investigation of measurement uncertainty of the velocity spectra is however out of the scope of the present study since a significantly larger number of samples would be required for that purpose.

The same conclusion applies for the lidar data at $z = 62$ m and $z = 61$ m, where the S_u spectrum is above the one estimated from the sonic anemometer on H-18 at $f_r \geq 0.1$. It is also unsure whether vortex shedding is visible in the S_v spectrum, especially at high frequencies, where the wind spectrum using the lidar data is expected to increase due to white noise in the Doppler spectra.

The measurement of the S_u and S_v spectra near the central part of the wake is challenged by the poorer performance of the lidar R2D3
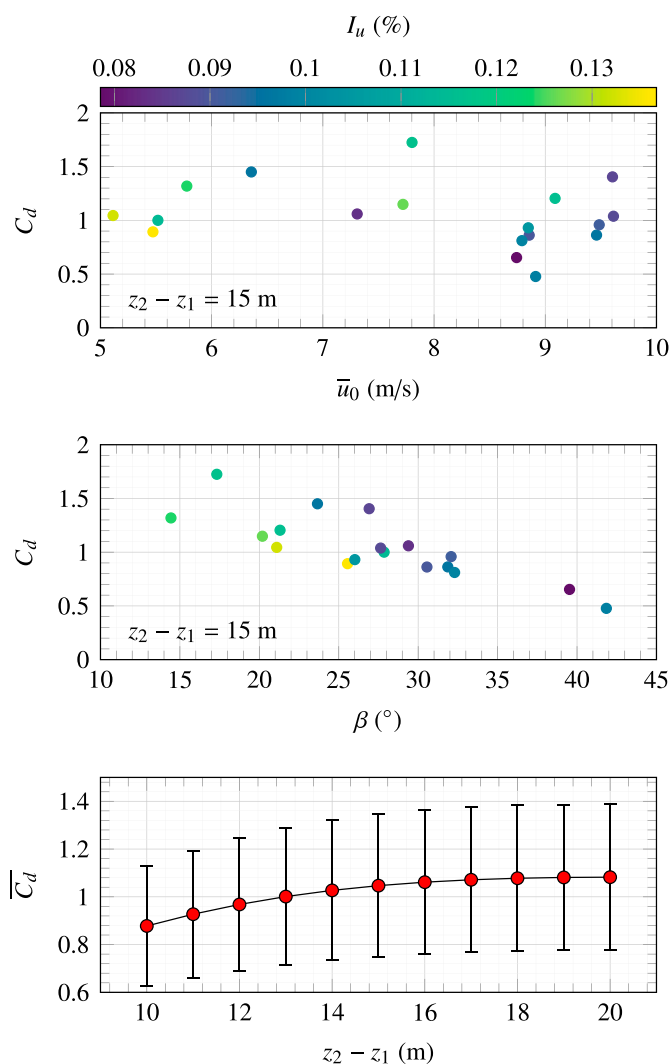
Fig. 11. Drag coefficient estimated for wind data recorded on 23/05/2014 from 01:00 to 07:50, expressed as a function of the undisturbed mean wind velocity (top) or the yaw angle (middle). The bottom panel shows the dependency of the averaged drag coefficient on the wake width.
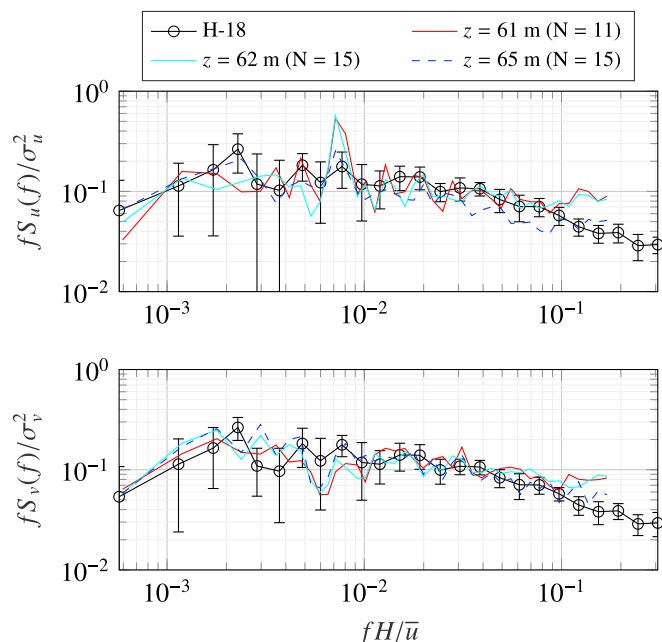
Fig. 12. Wind spectra recorded by the WindScanners on 23/05/2014 at three different altitudes, compared to the spectra obtained from the anemometer measurements on H-18. The number of available samples of 10 min duration is denoted N.

Fig. 13. Normalized along-beam wind velocity spectrum estimated using wind data recorded from 01:00 to 07:50 on 23/05/2014 with $\bar{v}_r(z = 65\,\text{m}) \geq 5\,\text{m s}^{-1}$ (19 samples), at each measurement height along the vertical line scanned by the WindScanner system.

compared to R2D1 in this area (Fig. 5). Using the data recorded by the lidar R2D1 only, it is possible to measure the spectrum of the along-beam wind component as a function of the measurement height. In Fig. 13, the spectrum S_{v_r} has been re-sampled using a logarithmic-spaced interval to improve its visualization in the low-frequency range. The spectrum S_{v_r} is here expressed as a function of the reduced frequency f_r (Eq. (15)). The mean wind velocity $\bar{u}(z)$ is estimated using the data recorded by the lidar R2D1 and the sonic anemometer, which provides information on the wind direction. Fluctuations of the wind direction with the height are expected, as illustrated in Fig. 6. Nonetheless, in a first approximation, $\bar{u}(z)$ is estimated in Fig. 13 using the wind direction at the sonic anemometer height only. At $z \approx 65$ m, the mean wind velocity is on average equal to 7.7 m s^{-1}.

The broad-banded vortex shedding is clearly visible in Fig. 13 at $f_r \geq 0.07$ and a height between ca. $z = 50$ m and $z = 60$ m. The wind spectra displayed suggest, therefore, that the data recorded between $z = 61$ m and $z = 62$ m are located in the upper part of the wake, which was unclear in Fig. 12. The existence of a clear peak near $f_r \approx 0.008$, at a height between $z = 55$ m and $z = 61$ m is, however, more surprising. The frequency at which this peak is observed is here equal to ca. 0.02 Hz, which is much lower than the eigenfrequencies of the bridge. The sonic anemometer on H-18 is located at $z \approx 62$ m, which likely explains why it does not record such a peak. The frequency of 0.02 Hz may be associated with the flow fluctuations generated by the tip of the Bergsholmen island. The Strouhal number of such a small island can be assumed equal to 0.21 (Thomson et al., 1977). Considering the averaged mean wind velocity during the recording period of ca. 8 m s^{-1} and the maximal height of the island that is 54 m, a vortex shedding frequency of 0.03 Hz is obtained, which is relatively close to the frequency observed in Fig. 13.

3.6. Challenges and prospects

The configuration used in the present pilot study suggests that the dynamic characteristics of the wake can be captured by the 2D-scanning short-range WindScanner system. In future applications, more detailed results may be achieved using a slightly different configuration than the one used here.
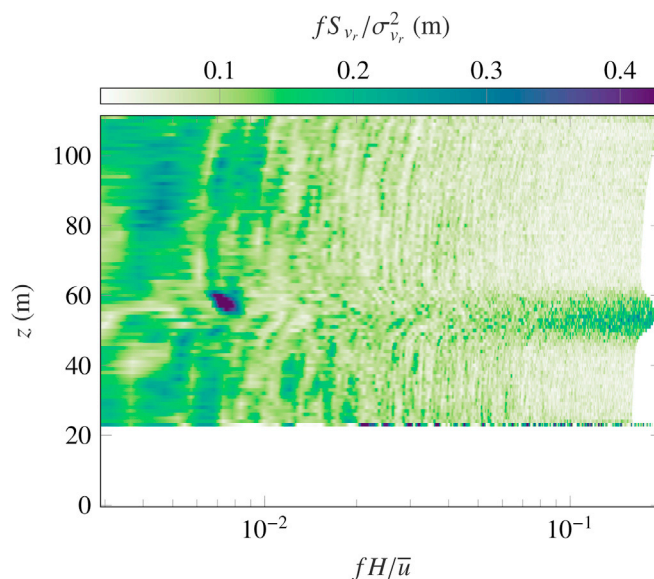
To take advantage of the small probe volume at short scanning distances, the distance between the vertical scanning beam and the bridge deck can be optimized. The scanned area was in the present case located at $x/H = 14.5$ from the deck, i.e. 14.5 times its height. The visualization of the wake may be optimal for $x/H \approx 3$, which is defined as the "very near wake" by Ong and Wallace (1996). At $r = 10$ m the Full Width at Half Maximum (FWHM) is only 13 cm, which also allows the study of the flow in the higher frequency range. This approach was for example used by van Dooren et al. (2016a) in a wind tunnel to study the wake downstream of scaled wind turbines. At lower scanning distances, the monitored area may, however, be in the dead zone of the lidar, i.e. too close from the instrument to be properly measured.

In the case of the Lysefjord Bridge, let's consider a scanning pattern along a vertical line segment, located at mid-span, at a distance $x/H = 3$. The beams of the two lidar units are forced to be orthogonal at zero elevation angle. The scanning distance for each lidar unit is denoted r_1 and r_2. The optimal location of the lidar units so that their FWHM is as small as possible is obtained by minimizing $r_1^2 + r_2^2$. This location corresponds to the case where the two lidar units are equidistant from the mid-span and are separated by ca. 16.6 m. In that case, the FWHM of both lidars is ca. 18 cm. Under this configuration, the maximal length of the vertical line segment is 20 m, which is likely large enough to capture the full wake structure at $x/H = 3$.

A shorter scanning distance is associated with larger elevation angles, which means that the influence of the vertical wind component on the measured radial velocity becomes non-negligible. In this situation, a system of three synchronized wind lidars (Mikkelsen et al., 2008a, b) is needed to properly retrieve the three wind components. However, it would require a more challenging installation to ensure that the three beams are as orthogonal to each other as possible. One solution may be to install the third lidar in-line with the vertical line segment and configure it to use a zenith-pointing mode as done by e.g. Lothon et al. (2006). For a bridge crossing a stretch of water, the deployment of the third lidar could be done using floating-lidar technology (Gottschall et al., 2017), however with the limitations regarding the observations, from a moving platform, of a small scale turbulence with a probe volume length of several meters.

4. Conclusions

A pilot study aiming to assess the applicability of a system of synchronized short-range wind lidars to measure the turbulent flow around a bridge deck in full-scale was conducted at the end of May 2014 on the Lysefjord bridge. During the last night of the measurement campaign, a stable atmospheric stratification associated with a favourable wind direction facilitated the first study of a bridge girder wake in full scale, using the short-range WindScanner system. The two lidar units scanned continuously the flow along a vertical line segment so that turbulence statistics could be investigated. The study led to the following findings:

- The high sampling frequency associated with the relatively small probe volume, which fluctuates between 5 m and 9 m in the present case, allows a visualization of the bridge wake with a time and spatial resolution high enough to estimate the velocity deficit in the bridge wake, even though the deck height is only 2.76 m and its width is 12.3 m.
- The drag coefficient deduced from the mean velocity deficit ranges from 0.88 to 1.08 and is in the overall agreement with the assumed design value of 1. The full-scale estimate was associated with a considerable variability due to the variable atmospheric conditions and the related wake width. Other contributing factors were the non-uniformity and unusual form of the vertical profile, such that the boundaries of the wake were not clearly identified.
- A broad-banded vortex shedding was observed for frequencies above 0.1 Hz. Although the turbulence intensity was much lower than usually recorded on the bridge, it was likely high enough so that the turbulent mixing prevented most of the time the shedding frequency from locking onto the eigenfrequencies of the bridge, and no vortex-induced vibration was clearly observed during the measurement period.
- A large spectral peak was observed in the lidar data for $56\,\text{m} \leq z \leq 62\,\text{m}$ at a frequency around 0.02 Hz, which is much lower than the eigenfrequencies of the bridge. The origin of such a peak might be related to the wake produced by the tip of the island of Bergsholmen, located 1 km upstream of the bridge.
- The use of two synchronized lidar units to measure the flow leads to a lower data availability than if a single lidar is used because missing data from one lidar unit propagates to the final retrieval of the velocities. This issue can be partly overcome with an efficient positioning of the lidar units, such that the lidar beams cross at an angle as close as possible to $90°$ and if the mean wind velocity recorded by each lidar unit is large enough.

Acknowledgements

References

Aitken, M.L., Banta, R.M., Pichugina, Y.L., Lundquist, J.K., 2014. Quantifying wind turbine wake characteristics from scanning remote sensor data. J. Atmos. Ocean. Technol. 31, 765–787. https://doi.org/10.1175/JTECH-D-13-00104.1.

Angelou, N., Foroughi Abari, F., Mann, J., Mikkelsen, T., Sjöholm, M., 2012a. Challenges in noise removal from Doppler spectra acquired by a continuous-wave lidar. In: 26th International Laser Radar Conference.

Angelou, N., Mann, J., Sjöholm, M., Courtney, M., 2012b. Direct measurement of the spectral transfer function of a laser based anemometer. Rev. Sci. Instrum. 83 https://doi.org/10.1063/1.3697728.

Bingöl, F., Mann, J., Larsen, G.C., 2010. Light detection and ranging measurements of wake dynamics part I: one-dimensional scanning. Wind energy 13, 51–61. https://doi.org/10.1002/we.352.

Chen, W.-L., Li, H., Hu, H., 2014. An experimental study on the unsteady vortices and turbulent flow structures around twin-box-girder bridge deck models with different

gap ratios. J. Wind Eng. Ind. Aerodyn. 132, 27–36. https://doi.org/10.1016/j.jweia.2014.06.015.

Cheynet, E., 2016. Wind-induced Vibrations of a Suspension Bridge: a Case Study in Full-scale. Ph.D. thesis. University of Stavanger, Norway.

Cheynet, E., Jakobsen, J.B., Snæbjörnsson, J., Mikkelsen, T., Sjöholm, M., Mann, J., Hansen, P., Angelou, N., Svardal, B., 2016. Application of short-range dual-Doppler lidars to evaluate the coherence of turbulence. Exp. Fluids 57, 184. https://doi.org/10.1007/s00348-016-2275-9.

Cheynet, E., Jakobsen, J.B., Snæbjörnsson, J., Reuder, J., Kumer, V., Svardal, B., 2017. Assessing the potential of a commercial pulsed lidar for wind characterisation at a bridge site. J. Wind Eng. Ind. Aerodyn. 161, 17–26. https://doi.org/10.1016/j.jweia.2016.12.002.

van Dooren, M., Kühn, M., Petrović, V., Bottasso, C., Campagnolo, F., Sjöholm, M., Angelou, N., Mikkelsen, T., Croce, A., Zasso, A., 2016a. Demonstration of synchronised scanning lidar measurements of 2d velocity fields in a boundary-layer wind tunnel. J. Phys. Conf. Ser. 072032. https://doi.org/10.1088/1742-6596/753/7/072032. IOP Publishing volume 753.

van Dooren, M.F., Trabucchi, D., Kühn, M., 2016b. A methodology for the reconstruction of 2d horizontal wind fields of wind turbine wakes based on dual-Doppler lidar measurements. Remote Sens. 8, 809. https://doi.org/10.3390/rs81008090.

Frandsen, J., 2001. Simultaneous pressures and accelerations measured full-scale on the Great Belt East suspension bridge. J. Wind Eng. Ind. Aerodyn. 89, 95–129. https://doi.org/10.1016/S0167-6105(00)00059-3.

Fransos, D., Bruno, L., 2010. Edge degree-of-sharpness and free-stream turbulence scale effects on the aerodynamics of a bridge deck. J. Wind Eng. Ind. Aerodyn. 98, 661–671. https://doi.org/10.1016/j.jweia.2010.06.008.

Fuertes, F.C., Iungo, G.V., Porté-Agel, F., 2014. 3d turbulence measurements using three synchronous wind lidars: validation against sonic anemometry. J. Atmos. Ocean. Technol. 31, 1549–1556.

Fujiwara, A., Kataoka, H., Ito, M., 1993. Numerical simulation of flow field around an oscillating bridge using finite difference method. J. Wind Eng. Ind. Aerodyn. 46–47, 567–575. https://doi.org/10.1016/0167-6105(93)90324-H. Proceedings of the 1st International on Computational Wind Engineering.

Gottschall, J., Gribben, B., Stein, D., Würth, I., 2017. Floating lidar as an advanced offshore wind speed measurement technique: current technology status and gap analysis in regard to full maturity. Wiley Interdiscip. Rev. Energy Environ. https://doi.org/10.1002/wene.250. E250 pp. e250–n/a.

Hjorth-Hansen, E., 1987. Askøy Bridge: Wind Tunnel Tests of Time-average Wind Loads for Box-girder Bridge Decks. SINTEF report STF71 A87037 SINTEF.

Iungo, G.V., Wu, Y.-T., Porté-Agel, F., 2013. Field measurements of wind turbine wakes with lidars. J. Atmos. Ocean. Technol. 30, 274–287. https://doi.org/10.1175/JTECH-D-12-00051.1.

Karlsson, C.J., Olsson, F.Å., Letalick, D., Harris, M., 2000. All-fiber multifunction continuous-wave coherent laser radar at 1.55 μm for range, speed, vibration, and wind measurements. Appl. Opt. 39, 3716–3726. https://doi.org/10.1364/AO.39.003716.

Käsler, Y., Rahm, S., Simmet, R., Kühn, M., 2010. Wake measurements of a multi-MW wind turbine with coherent long-range pulsed Doppler wind lidar. J. Atmos. Ocean. Technol. 27, 1529–1532. https://doi.org/10.1175/2010JTECHA1483.1.

Kuroda, S., 1997. Numerical simulation of flow around a box girder of a long span suspension bridge. J. Wind Eng. Ind. Aerodyn. 67 – 68, 239–252. https://doi.org/10.1016/S0167-6105(97)00076-7. Computational Wind Engineering.

Lange, J., Mann, J., Angelou, N., Berg, J., Sjöholm, M., Mikkelsen, T., 2015. Variations of the wake height over the Bolund escarpment measured by a scanning lidar. Bound. Layer Meteorol. 159, 147–159. https://doi.org/10.1007/s10546-015-0107-8.

Li, H., Laima, S., Zhang, Q., Li, N., Liu, Z., 2014. Field monitoring and validation of vortex-induced vibrations of a long-span suspension bridge. J. Wind Eng. Ind. Aerodyn. 124, 54–67. https://doi.org/10.1016/j.jweia.2013.11.006.

Lothon, M., Lenschow, D., Mayor, S., 2006. Coherence and scale of vertical velocity in the convective boundary layer from a Doppler lidar. Bound. Layer Meteorol. 121, 521–536. https://doi.org/10.1007/s10546-006-9077-1.

Mann, J., Cariou, J.-P., Courtney, M.S., Parmentier, R., Mikkelsen, T., Wagner, R., Lindelöw, P., Sjöholm, M., Enevoldsen, K., 2009. Comparison of 3D turbulence measurements using three staring wind lidars and a sonic anemometer. Meteorol. Z. 18, 135–140. https://doi.org/10.1127/0941-2948/2009/0370.

Mikkelsen, T., 2014. Lidar-based research and innovation at dtu wind energy–a review. J. Phys. Conf. Ser. https://doi.org/10.1088/1742-6596/524/1/012007. IOP Publishing volume 524.

Mikkelsen, T., Courtney, M., Antoniou, I., Mann, J., 2008a. Wind scanner: a full-scale laser facility for wind and turbulence measurements around large wind turbines. In: Conference Proceedings (Online). European Wind Energy Association (EWEA).

Mikkelsen, T., Mann, J., Courtney, M., Sjöholm, M., 2008b. Windscanner: 3-D wind and turbulence measurements from three steerable Doppler lidars. IOP Conf. Ser. Earth Environ. Sci. 1, U148–U156. https://doi.org/10.1088/1755-1307/1/1/012018.

Narasimhamurthy, V.D., Andersson, H.I., 2009. Numerical simulation of the turbulent wake behind a normal flat plate. Int. J. Heat Fluid Flow 30, 1037–1043. https://doi.org/10.1016/j.ijheatfluidflow.2009.09.002.

Newsom, R., Calhoun, R., Ligon, D., Allwine, J., 2008. Linearly organized turbulence structures observed over a suburban area by dual-Doppler lidar. Bound. Layer Meteorol. 127, 111–130. https://doi.org/10.1007/s10546-007-9243-0.

Newsom, R.K., Berg, L.K., Shaw, W.J., Fischer, M.L., 2015. Turbine-scale wind field measurements using dual-Doppler lidar. Wind Energy 18, 219–235. https://doi.org/10.1002/we.1691.

Obukhov, A., 1946. Turbulence in thermally inhomogeneous atmosphere. Tr. Inst. Teor. Geofiz. Akad. Nauk. SSSR 1, 95–115.

Ong, L., Wallace, J., 1996. The velocity field of the turbulent very near wake of a circular cylinder. Exp. Fluids 20, 441–453. https://doi.org/10.1007/BF00189383.

Pearson, R., 2005. Mining Imperfect Data: Dealing with Contamination and Incomplete Records. SIAM e-books. Society for Industrial and Applied Mathematics (SIAM).

Peña, A., Bechmann, A., Conti, D., Angelou, N., 2016. The fence experiment–full-scale lidar-based shelter observations. Wind Energy Sci. 1, 101–114. https://doi.org/10.5194/wes-1-101-2016.

Priestley, M.B., 1965. Evolutionary spectra and non-stationary processes. J. R. Stat. Soc. Ser. B Methodol. 27, 204–237. http://www.jstor.org/stable/2984191.

Sjöholm, M., Angelou, N., Hansen, P., Hansen, K.H., Mikkelsen, T., Haga, S., Silgjerd, J.A., Starsmore, N., 2014. Two-dimensional rotorcraft downwash flow field measurements by lidar-based wind scanners with agile beam steering. J. Atmos. Ocean. Technol. 31, 930–937. https://doi.org/10.1175/JTECH-D-13-00010.1.

Sjöholm, M., Mikkelsen, T., Mann, J., Enevoldsen, K., Courtney, M., 2009. Spatial averaging-effects on turbulence measured by a continuous-wave coherent lidar. Meteorol. Z. 18, 281–287. https://doi.org/10.1127/0941-2948/2009/0379.

Solari, G., Piccardo, G., 2001. Probabilistic 3-D turbulence modeling for gust buffeting of structures. Probab. Eng. Mech. 16, 73–86. https://doi.org/10.1016/S0266-8920(00)00010-2.

Teunissen, H., 1980. Structure of mean winds and turbulence in the planetary boundary layer over rural terrain. Bound. Layer Meteorol. 19, 187–221. https://doi.org/10.1007/BF00117220.

Thomson, R.E., Gower, J.F., Bowker, N.W., 1977. Vortex streets in the wake of the Aleutian islands. Mon. Weather Rev. 105, 873–884. https://doi.org/10.1175/1520-0493(1977)105<0873:VSITWO>2.0.CO;2.

Thyng, K.M., Greene, C.A., Hetland, R.D., Zimmerle, H.M., DiMarco, S.F., 2016. True colors of oceanography: guidelines for effective and accurate colormap selection. Oceanography 29, 9–13. https://doi.org/10.5670/oceanog.2016.66.

Trujillo, J.-J., Bingöl, F., Larsen, G.C., Mann, J., Kühn, M., 2011. Light detection and ranging measurements of wake dynamics. Part II: two-dimensional scanning. Wind Energy 14, 61–75. https://doi.org/10.1002/we.402.

Welch, P.D., 1967. The use of fast Fourier transform for the estimation of power spectra: a method based on time averaging over short, modified periodograms. IEEE Trans. Audio Electroacoust. 15, 70–73. https://doi.org/10.1109/TAU.1967.1161901.

Wilczak, J.M., Oncley, S.P., Stage, S.A., 2001. Sonic anemometer tilt correction algorithms. Bound. Layer Meteorol. 99, 127–150. https://doi.org/10.1023/A:1018966204465.

Yang, Y., Zhou, R., Ge, Y., Mohotti, D., Mendis, P., 2015. Aerodynamic instability performance of twin box girders for long-span bridges. J. Wind Eng. Ind. Aerodyn. 145, 196–208. https://doi.org/10.1016/j.jweia.2015.06.014.

Zhu, L., Xu, Y., Zhang, F., Xiang, H., 2002. Tsing Ma bridge deck under skew winds – Part I: aerodynamic coefficients. J. Wind Eng. Ind. Aerodyn. 90, 781–805. https://doi.org/10.1016/S0167-6105(02)00160-5.